Composites Science and Technology
March 2008, Volume 68, Issues 3-4, Pages 1015-1024
http://dx.doi.org/10.1016/j.compscitech.2007.07.020

Influence of winding pattern on the mechanical behavior of filament wound composite cylinders under external pressure

H. Hernández-Morenoa[b], B. Douchin[a, *], F. Collombet[a], D. Choqueuse[c] and P. Davies[c]

[a] Laboratoire de Génie Mécanique de Toulouse, PRO2COM, IUT Paul Sabatier, 133c Avenue de Rangueil, BP 61701, 31077 Toulouse Cedex 4, France
[b] Instituto Politécnico Nacional, ESIME Unidad Ticomán, Av. Ticomán No. 600, Col. San José Ticomán, 07340 México D.F., Mexico
[c] IFREMER Materials & Structures Group, Brest Centre, BP70, 29280 Plouzané, France

*: Corresponding author : B. Douchin, email address : bernard.douchin@iut-tlse3.fr

Abstract:

The influence of winding pattern on the mechanical response of filament wound glass/epoxy cylinders exposed to external pressure is studied by testing cylindrical specimens having stacked layers with coincident patterns in a hyperbaric testing chamber. Different analytical models are evaluated to predict buckling pressure and modes of thin wall cylinders (diameter to thickness ratio d/h of 25) and satisfactory predictions are obtained which are in the same order of magnitude that those obtained in experimental results. Test results show no evident pattern influence on either strength (implosion pressure) or buckling behavior (buckling modes) of thin wall or thick wall (d/h of 10) cylinders.

Keywords: A. Polymer-matrix composites; E. Filament winding; C. Buckling; C. Cylindrical shells

1. Introduction

Marine and oceanographic research uses unmanned instrumented vessels for deep ocean research; some of them are made using composite materials and fabricated by the filament winding process. These vessels are mainly exposed to external pressure during service. Design and analysis practices for this kind of structure use the main assumptions of classical laminate theory [1]. In reality the reinforcement structure of filament wound cylinders is more complex than a classical laminate, because fibres form a pattern which is absent in laminates. These patterns have some zones of undulations and others where the material can be considered as a laminate. Filament wound

composite cylinders may have different reinforcement patterns but the same global physical characteristics, such as volume fractions, thickness and number of layers. Several works have been made in order to evaluate these properties as a function of process parameters, a remarkable research is the one made by Koussios [2], other researches concern modification of FEM packages by taking in to account process parameters, this is the case in the work of Zhao et al [3].

The present work investigates the influence of pattern architecture and dimensions on the mechanical behaviour, under external pressure, of filament wound cylinders. Such an influence may be revealed by a loss of strength or by a change in buckling or failure modes.

Among the many research papers dealing with buckling of cylindrical shells, those of Donnell [4], Flügge [5], and Cheng and Ho [6] are regularly cited. Several studies have shown that buckling behaviour is sensitive to geometrical defects. These defects may be thickness variations due to the fabrication process. Modification of buckling theories to take into account geometrical defects on the cylinder wall was studied for example by Peterson et al [7], Tennyson and Smithses [8] in the 1970's and 80's and Fuchs et al [9]. In the 90's, there is the work of Hahn et al [10] concerning compression buckling and Messager [11] concerning thickness defects on external pressure buckling behaviour. In those studies, imperfections were taken into account as axial thickness harmonic variations. Imperfection sensitivities of naval structures have been studied by Elghazouli et al [12] who performed compression. In the same way, Carvelli et al [13] tested buckling behaviour for technological demonstrators at sea. Those studies are based, mainly, on experimental measurement of thickness or surface topography, some of them also represent reinforcement structure through a thickness variation, but in filament wound cylinders material heterogeneity is not necessarily coupled with thickness variation.

Hahn et al [10] observed a dependency of buckling modes on winding pattern: when pattern size was similar to the expected buckling mode, the critical buckling stress reached a minimum value, Although that work deals with pattern influence on composite cylinders [10] under uniaxial compression loading, one might suppose that a similar pattern sensitivity exists for biaxial compression (external pressure). In order to examine this, in the present study, a series of implosion tests was carried out in a hyperbaric chamber, on cylindrical specimens of two pattern sizes and two wall thicknesses, made of continuous

glass roving and epoxy resin. In parallel, several theoretical models to predict buckling pressure and buckling modes have been evaluated.

In the present paper, the winding pattern architecture produced by the filament winding process is presented first. Next, an evaluation of several models is presented using theoretical properties and, finally, results from axial compression and hyperbaric implosion tests are presented.

2. Winding and pattern architecture

The filament winding process consists of winding a glass roving around a cylindrical mandrel. The roving is impregnated with resin before being wound, and roving tension can be adjusted in order to control composite compaction. The roving dispenser displacement and mandrel rotation are synchronized by numerical control equipment similar to that used in machine tools.

This fabrication process can produce three types of winding, circumferential, helical and polar [14] [15] [16] [17]. Here, only the pattern produced by helical winding is treated.

Helical trajectories are used for winding angles between 5 and 80°. With this type of winding it is possible to cover cylindrical or conical surfaces but it is not adapted to cover extremities, for example hemispherical ends [17].

For this type of winding, the machine used is horizontal, normally with three degrees of freedom: axial, radial and rotation around the central axis (see Figure 1).

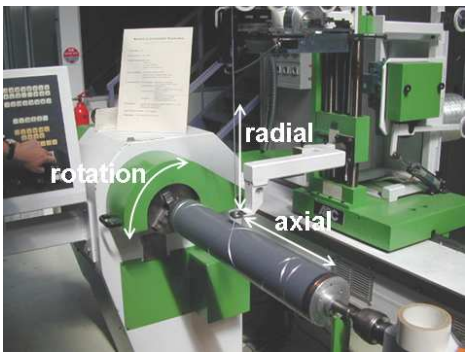

Fig. 1. Filament winding machine (LGMT PRO^{2}COM) and its displacements.

This type of machine has a carriage which moves in the axial direction and is provided with a roving feed system [18]. Roving is wound over the mandrel which turns at the same time as the machine spindle. Combined rotational and axial movements produce double helical trajectories and a rhomboid shape pattern (see Figure 2). When the entire surface is covered, there is, in reality, a double weave ply layer, equivalent in volume to two unidirectional layers.

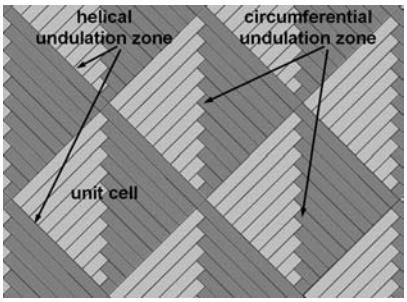

Fig. 2. Rhomboid pattern architecture produced by helical winding.

Within each rhomboid, one can distinguish two parts each one comprising half of the rhomboid and having one edge with a unidirectional layer. Between both parts there is a circumferential undulation zone where rovings cross over. At each rhomboid side, there is a helical undulation zone. Each rhomboid constitutes a minimal periodical structure forming the winding pattern, which can be called the unit cell (see Figure 2). Detailed information about kinematics and its relationship with design and fabrication can be found in Koussios [2].

3. Specimen characteristics and conditioning

Cylindrical specimens used in this research were 350 mm long, 125 mm internal diameter, thickness 4.4 mm (thin walled) or 12.6 mm (thick walled), 250 mm long in the central parallel section, and with a 90° winding reinforced section at both extremities. Dimensions are presented on Figure 3. Winding angle in the central section has a value of ±55°, which is a classical winding angle for pressure vessels, where hoop stress is twice the value of axial stress. Two pattern architectures were selected, 1 or 5 unit cells along the circumference (see Figure 4). Specimens were fabricated using a 3.5 mm width continuous roving. The resin system was LY 5052 / HY 5052.

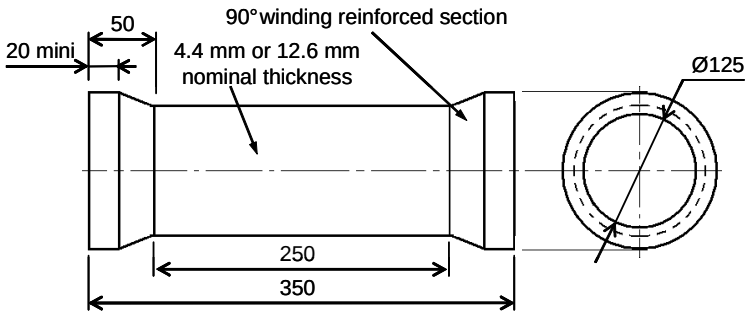

Fig.3. Specimen dimensions.

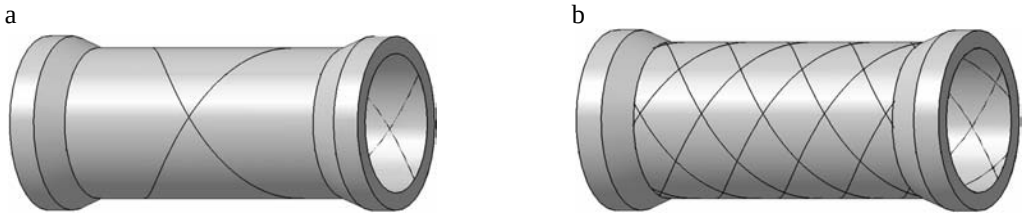

Fig. 4. Specimens showing pattern architecture; (a) 1 unit cell pattern, (b) 5 unit cell pattern.

Layer patterns were placed to be stacked coincident through the thickness direction, in order to amplify possible unit cell size influence on mechanical behaviour. Winding angle was strictly maintained for all layers, this produced a slight increase in cell size with thickness. Mean measured thicknesses were 4.4 mm and 12.6 mm for thin walled and thick walled cylinders respectively. The standard deviation for thin walled cylinders is 0.16 mm and for thick cylinders is 0.26 mm. Once specimens were wound and cured, at 50°C for 15 hours, both extremities were machined flat, in order to obtain final dimensions. Fiber volumetric fractions were obtained by burn off method, giving a mean of 51% with a standard deviation of 2.1%.

4. Buckling analysis

4.1 Mechanical properties

Mechanical properties and constitutive relations are initially calculated, in order to have a first approach for the cylinder's behavior, taking into account as much as possible the winding architecture. For this, a unit cell is the starting point (see Figure 5). As was stated in the previous section, the filament winding unit cell is actually formed by two layers, each layer has balanced fiber orientations, half of the volume of each layer shows a fiber orientation $+\alpha$ and the other half $-\alpha$, as shown in Figure 5. This characteristic

allows a filament wound layer to be considered as composed of two unidirectional plies both acting together as an orthotropic layer without extension - bending nor extension - torsion coupling.

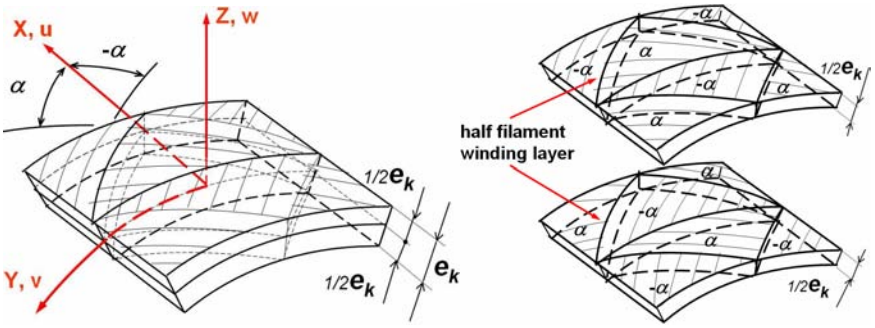

Fig. 5. Component zones in a filament winding unit cell.

The stiffness matrix for a filament wound layer can be obtained from individual stiffness matrices of equivalent unidirectional component layers by a rule of mixtures considering each unidirectional layer as having a volume fraction of 0.5 and using equation 1, because a filament winding layer has two fiber directions (+55° and -55°) crossed and superposed like a textile composite, where 50% of fibers are lying in one direction and 50% in the other direction.

$$(Q_{ij})_{fw} = \sum_{k=1}^{k=2} V_k (Q_{ij})_k \tag{1}$$

where $(Q_{ij})_k$ is the stiffness matrix element *ij* of the *k* unidirectional layer, and $(Q_{ij})_{fw}$ is the stiffness matrix element *ij* of the filament wound layer.

The shell constitutive relationships can be obtained using classical laminate theory. Knowing already that each filament wound layer is orthotropic, the shell constitutive relation can be written as:

$$\begin{bmatrix} N_x \\ N_y \\ N_{xy} \\ M_x \\ M_y \\ M_{xy} \end{bmatrix} = \begin{bmatrix} A_{11} & A_{12} & 0 & 0 & 0 & 0 \\ A_{21} & A_{22} & 0 & 0 & 0 & 0 \\ 0 & 0 & A_{66} & 0 & 0 & 0 \\ 0 & 0 & 0 & D_{11} & D_{12} & 0 \\ 0 & 0 & 0 & D_{21} & D_{22} & 0 \\ 0 & 0 & 0 & 0 & 0 & D_{66} \end{bmatrix} \begin{bmatrix} \varepsilon_x^0 \\ \varepsilon_y^0 \\ \gamma_{xy}^0 \\ \kappa_x \\ \kappa_y \\ \kappa_{xy} \end{bmatrix} \tag{2}$$

where N_i is the force / unit length acting on the shell in the i direction, and M_i is the moment / unit length acting on the shell in direction i. ε^0_i is the membrane strain following i direction, and κ_i is the shell curvature in the i direction. Elements of the shell stiffness matrix can be obtained using equations 3 and 4:

$$A_{ij} = \sum_{k=1}^{k=n} (h_k - h_{k-1})(Q_{ij})_{fw} \tag{3}$$

$$D_{ij} = \frac{1}{3}\sum_{k=1}^{k=n} (h_k^3 - h_{k-1}^3)(Q_{ij})_{fw} \tag{4}$$

where h_k is the through thickness position of the layer within the laminate, the laminated stacking sequence is sketched in Figure 6.

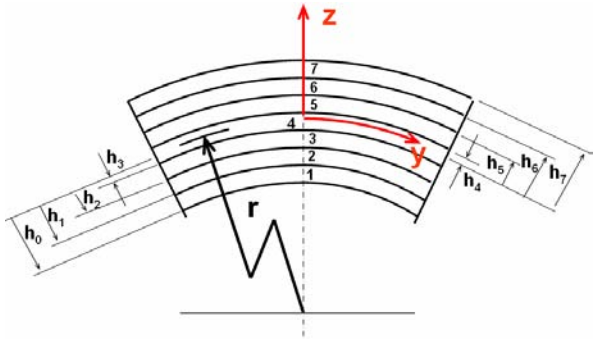

Fig. 6. Stacking sequence and layer position.

Table 1
Mechanical properties of unidirectional layer [19]

E_1 *(MPa)*	39000
E_2 *(MPa)*	8600
ν_{12}	0.28
ν_{21}	0.0617
G_{12} *(MPa)*	3800

Considering the properties of an unidirectional layer presented in Table 1, taken from reference [19], the shell constitutive relations can be evaluated numerically, first by obtaining individual stiffness matrices of each unidirectional layer, applying equation 5, considering that E_i is the Young's modulus in the i direction, ν_{12} and ν_{21} are the axial and circumferential Poisson ratios respectively and G_{12} is the shear

modulus of the shell, where 1 and 2 are the principal directions in the unidirectional ply. The reference coordinate system is shown on Figure 7.

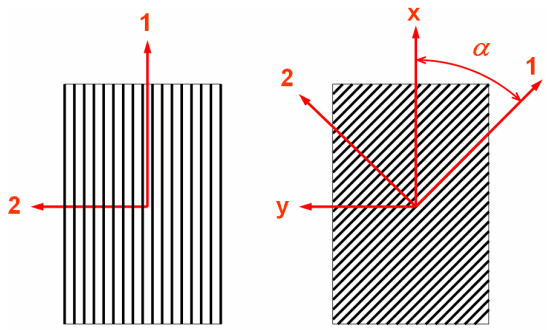

Fig. 7. Layer orientation with respect to cylinder coordinates.

$$[Q]_{12} = \begin{bmatrix} \frac{E_1}{1-\nu_{12}\nu_{21}} & \frac{\nu_{21}E_1}{1-\nu_{12}\nu_{21}} & 0 \\ \frac{\nu_{12}E_2}{1-\nu_{12}\nu_{21}} & \frac{E_2}{1-\nu_{12}\nu_{21}} & 0 \\ 0 & 0 & G_{12} \end{bmatrix} \tag{5}$$

Equation 5 is written following principal directions (see Figure 7), so these equations must be transformed in directions following the composite shell axial and circumferential directions (see Figures 5 and 7). After transformations the stiffness matrix of each individual unidirectional layer can be written as below, equations 6 and 7:

$$[Q]_{xy(\theta=55°)} = \begin{bmatrix} 12673 & 8706 & -4990 \\ 8706 & 23253 & -9544 \\ -4990 & -9544 & 10055 \end{bmatrix} \tag{6}$$

$$[Q]_{xy(\theta=-55°)} = \begin{bmatrix} 12673 & 8706 & 4990 \\ 8706 & 23253 & 9544 \\ 4990 & 9544 & 10055 \end{bmatrix} \tag{7}$$

Now using equation 1, the filament wound layer stiffness matrix becomes (equation 8):

$$[Q]_{xy(fw)} = \begin{bmatrix} 12673 & 8706 & 0 \\ 8706 & 23253 & 0 \\ 0 & 0 & 10055 \end{bmatrix} \tag{8}$$

Using the shell stacking sequence and the positions described in Table 2, and equations 3 and 4, the shell constitutive relation elements (A_{ij} and D_{ij}) are calculated and presented in Table 3.

Table 2

Specimen layer geometrical data

layer k	orientation θ_k (°)	thickness e_k (mm)	h_k (mm)	h_{k-1} (mm)
1	±55	0.63	-1.575	-2.205
2	±55	0.63	-0.945	-1.575
3	±55	0.63	-0.315	-0.945
4	±55	0.63	0.315	-0.315
5	±55	0.63	0.945	0.315
6	±55	0.63	1.575	0.945
7	±55	0.63	2.205	1.575

Table 3

Calculated and experimental *A* and *D* constant values

Elastic constants	Calculated *A* (N/mm) and *D* values (Nmm)	Experimental *A* (N/mm) and *D* (Nmm) values
A_{11}	55888	59857
A_{12}	38393	36909
A_{21}	38393	36936
A_{22}	102547	98965
A_{66}	44345	44345
D_{11}	90577	97009
D_{12}	62222	59818
D_{21}	62222	59862
D_{22}	166196	160390
D_{66}	71868	71868 (calculated value)

4.2 Calculated buckling modes and pressure

Buckling modes and pressures were calculated using several different cylindrical shell buckling models from the literature, those models are: Flügge's model [5], a modified Flügge model [20], the Cheng and Ho model [6], the Donnell model [4], and a modified version of Sanders' model proposed by Messager [11].

For each model, equilibrium equations are presented, as well as kinematic relationships and a proposed buckling solution. Nomenclature and the meaning of variables are presented schematically in Figure 8, where equilibrium of forces and moments in a cylindrical shell differential element are represented.

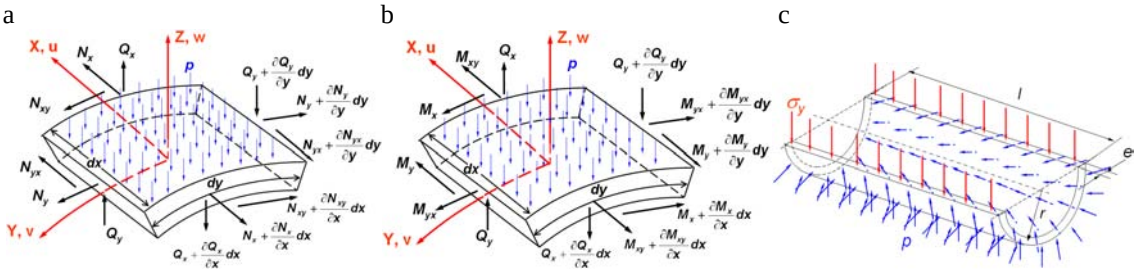

Fig. 8. Shell differential element equilibrium; (a) force equilibrium, (b) moment equilibrium, (c) pressure acting on shell.

Equilibrium equations of the modified Flügge model [20] [5] are presented in equations 9 to 11.

$$\frac{\partial N_x}{\partial x}+\frac{\partial N_{yx}}{\partial y}-p\left[\frac{\partial w}{\partial x}+r\frac{\partial^2 v}{\partial x\partial y}\right]=0 \tag{9}$$

$$\frac{\partial N_{xy}}{\partial x}+\frac{\partial N_y}{\partial y}+\frac{1}{r}\frac{\partial M_y}{\partial y}+\frac{1}{r}\frac{\partial M_{xy}}{\partial x}-p\left[\frac{\partial w}{\partial y}+\frac{1}{2}r\frac{\partial^2 u}{\partial y\partial x}\right]=0 \tag{10}$$

$$\frac{\partial^2 M_y}{\partial y^2}+2\frac{\partial^2 M_{xy}}{\partial y\partial x}+\frac{\partial^2 M_x}{\partial x^2}-\frac{N_y}{r}-p\left[\frac{1}{2}r\frac{\partial^2 w}{\partial x^2}+r\frac{\partial^2 w}{\partial y^2}\right]=0 \tag{11}$$

where *u*, *v* and *w* are the shell displacements following axial, circumferential and radial directions, *r* is the shell radius (radius of the median shell surface), and *p* is the external pressure acting on the shell (see Figure 8).

For this model kinematic relationships are given by equations 12 to 17:

$$\varepsilon_x^0=\frac{\partial u}{\partial x} \tag{12}$$

$$\varepsilon_y^0=\frac{\partial v}{\partial y}+\frac{w}{r} \tag{13}$$

$$\gamma_{xy}^0=\frac{\partial u}{\partial y}+\frac{\partial v}{\partial x} \tag{14}$$

$$\kappa_x = -\frac{\partial^2 w}{\partial x^2} \tag{15}$$

$$\kappa_y = -\frac{\partial^2 w}{\partial y^2} + \frac{w}{r^2} \tag{16}$$

$$\kappa_{xy} = -2\frac{\partial^2 w}{\partial x \partial y} - \frac{1}{r}\frac{\partial u}{\partial y} + \frac{1}{r}\frac{\partial v}{\partial x} \tag{17}$$

The proposed solution is the system of equations from 18 to 20 and the reference coordinate system for this model is presented in Figure 9.

$$u = U\,sin\left(\frac{m\pi x}{L}\right)sin\left(\frac{ny}{r}\right) \tag{18}$$

$$v = V\,cos\left(\frac{m\pi x}{L}\right)cos\left(\frac{ny}{r}\right) \tag{19}$$

$$w = W\,cos\left(\frac{m\pi x}{L}\right)sin\left(\frac{ny}{r}\right) \tag{20}$$

where U, V and W are amplitudes of displacements u, v, w respectively, m is the number of half weaves in the axial direction, and n is the number of weaves in the circumferential direction.

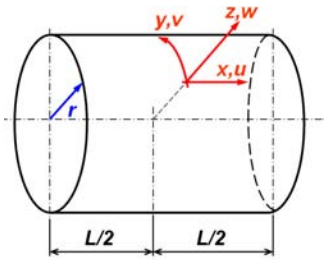

Fig. 9. Coordinate system for the modified Flügge model.

For the Flügge model, the equilibrium equations are:

$$\frac{\partial N_x}{\partial x} + \frac{\partial N_{yx}}{\partial y} - p\left[r\frac{\partial^2 u}{\partial y^2} - \frac{\partial w}{\partial x} + \frac{r}{2}\frac{\partial^2 u}{\partial x^2}\right] = 0 \tag{21}$$

$$\frac{\partial N_{xy}}{\partial x} + \frac{\partial N_y}{\partial y} + \frac{1}{r}\frac{\partial M_y}{\partial y} + \frac{1}{r}\frac{\partial M_{xy}}{\partial x} - p\left[r\frac{\partial^2 v}{\partial y^2} + \frac{\partial w}{\partial y} + \frac{r}{2}\frac{\partial^2 v}{\partial x^2}\right] = 0 \tag{22}$$

$$\frac{\partial^2 M_y}{\partial y^2}+2\frac{\partial^2 M_{xy}}{\partial y\partial x}+\frac{\partial^2 M_x}{\partial x^2}-\frac{N_y}{r}-p\left[\frac{\partial u}{\partial x}-\frac{\partial v}{\partial y}+r\frac{\partial^2 w}{\partial y^2}+\frac{r}{2}\frac{\partial^2 w}{\partial x^2}\right]=0 \tag{23}$$

The kinematic relationships are the same as in the modified Flügge model (equations from 13 to 17), the solution proposed is presented in equations from 24 to 26, and the coordinate system is presented in Figure 10.

$$u=U\cos\left(\frac{m\pi x}{L}\right)\cos\left(\frac{ny}{r}\right) \tag{24}$$

$$v=V\sin\left(\frac{m\pi x}{L}\right)\sin\left(\frac{ny}{r}\right) \tag{25}$$

$$w=W\sin\left(\frac{m\pi x}{L}\right)\cos\left(\frac{ny}{r}\right) \tag{26}$$

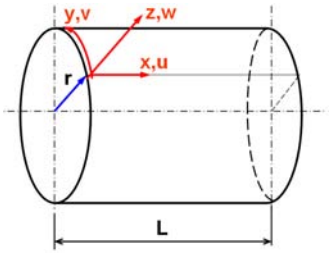

Fig. 10. Coordinate system for Flügge model.

For the model presented by Cheng and Ho, the equilibrium equations are the same as in Flügge's model with a difference in the last equation, which is modified and takes the form of equation 27. The kinematic relations are the same as for the Flügge model:

$$\frac{\partial^2 M_y}{\partial y^2}+\frac{\partial^2 M_{xy}}{\partial y\partial x}+\frac{\partial^2 M_{yx}}{\partial y\partial x}+\frac{\partial^2 M_x}{\partial x^2}-\frac{N_y}{r}-p\left[\frac{\partial u}{\partial x}-\frac{\partial v}{\partial y}+r\frac{\partial^2 w}{\partial y^2}+\frac{r}{2}\frac{\partial^2 w}{\partial x^2}\right]=0 \tag{27}$$

Here the constitutive relations are different however; this model uses the constitutive relations presented in equation 28.

$$\begin{bmatrix} N_x \\ N_y \\ N_{xy} \\ N_{yx} \\ M_x \\ M_y \\ M_{xy} \\ M_{yx} \end{bmatrix} = \begin{bmatrix} A_{11} & A_{12} & 0 & \frac{D_{11}}{r} & 0 & 0 \\ A_{12} & A_{22} & 0 & 0 & \frac{D_{22}}{r} & 0 \\ 0 & 0 & A_{66}+\frac{D_{66}}{2r^2} & 0 & 0 & \frac{D_{66}}{2r} \\ 0 & 0 & A_{66}+\frac{D_{66}}{2r^2} & 0 & 0 & -\frac{D_{66}}{2r} \\ \frac{D_{11}}{r} & \frac{D_{12}}{r} & \frac{D_{16}}{r} & D_{11} & D_{12} & 0 \\ 0 & 0 & 0 & D_{12} & D_{22} & 0 \\ 0 & 0 & \frac{D_{66}}{r} & 0 & 0 & D_{66} \\ 0 & 0 & 0 & 0 & 0 & D_{66} \end{bmatrix} \begin{bmatrix} \varepsilon_x^0 \\ \varepsilon_y^0 \\ \gamma_{xy}^0 \\ \kappa_x \\ \kappa_y \\ \kappa_{xy} \end{bmatrix} \tag{28}$$

The proposed solution is given by equations from 29 to 31, with a coordinate system shown in Figure 9.

$$u_0 = A\,sin\left(\frac{m\pi x}{L}+\frac{ny}{r}\right) \tag{29}$$

$$v_0 = B\,sin\left(\frac{m\pi x}{L}+\frac{ny}{r}\right) \tag{30}$$

$$w_0 = C\,cos\left(\frac{m\pi x}{L}+\frac{ny}{r}\right) \tag{31}$$

For Donnell's model the equilibrium equations are:

$$\frac{\partial N_x}{\partial x}+\frac{\partial N_{yx}}{\partial y}-p\left[r\frac{\partial^2 u}{\partial y^2}-\frac{\partial w}{\partial x}+\frac{r}{2}\frac{\partial^2 u}{\partial x^2}\right]=0 \tag{32}$$

$$\frac{\partial N_{xy}}{\partial x}+\frac{\partial N_y}{\partial y}-p\left[r\frac{\partial^2 v}{\partial y^2}+\frac{\partial w}{\partial y}+\frac{r}{2}\frac{\partial^2 v}{\partial x^2}\right]=0 \tag{33}$$

$$\frac{\partial^2 M_y}{\partial y^2}+2\frac{\partial^2 M_{xy}}{\partial y\partial x}+\frac{\partial^2 M_x}{\partial x^2}-\frac{N_y}{r}-p\left[\frac{\partial u}{\partial x}-\frac{\partial v}{\partial y}+r\frac{\partial^2 w}{\partial y^2}+\frac{r}{2}\frac{\partial^2 w}{\partial x^2}\right]=0 \tag{34}$$

The kinematic relationships are the same as those used in the modified Flügge model (equations from 12 to 17), and the proposed solution is the same as that used in the Cheng and Ho model (equations 29 to 31). The reference coordinate system is presented in Figure 9.

The modified Sanders model used by Messager has the equilibrium equations presented in equations:

$$\frac{\partial N_x}{\partial x}+\frac{\partial N_{xy}}{\partial y}=0 \tag{35}$$

$$\frac{\partial N_y}{\partial y}+\frac{\partial N_{xy}}{\partial x}+\frac{1}{r}\frac{\partial M_y}{\partial y}+\frac{1}{r}\frac{\partial M_{xy}}{\partial x}+\frac{p}{r}\left[v-r\frac{\partial w}{\partial y}\right]=0 \tag{36}$$

$$\frac{\partial^2 M_x}{\partial x^2}+2\frac{\partial^2 M_{xy}}{\partial x\partial y}+\frac{\partial^2 M_y}{\partial y^2}-\frac{N_y}{R}-p\left[\frac{r}{2}\frac{\partial^2 w}{\partial x^2}+r\frac{\partial^2 w}{\partial y^2}-\frac{\partial v}{\partial y}\right]=0 \tag{37}$$

The kinematic relations are equations from 12 to 15, and for curvatures y and xy equations are those referenced by 38 and 39. The solution proposed is formed by equations from 24 to 26, and the coordinate system used is presented in Figure 10.

$$\kappa_y=-\frac{\partial^2 w}{\partial y^2}+\frac{1}{r}\frac{\partial v}{\partial y} \tag{38}$$

$$\kappa_{xy}=-2\frac{\partial^2 w}{\partial x\partial y}+\frac{2}{r}\frac{\partial v}{\partial x} \tag{39}$$

For each model the substitution of proposed solutions into the kinematical relations, and then into constitutive equations, and finally into the equilibrium equations, gives a system of equations with 3 unknown amplitudes *U*, *V*, *W* and external pressure *p*. The solution of this equation system for *p*, gives an expression depending on shell stiffness constants A_{ij}, D_{ij}, *m* and *n*. A_{ij} and D_{ij} are already known. The critical pressure is obtained by an iterative search using given values for *m* and *n*, until finding the minimum value for *p*, this *p* value is the critical pressure and the *m* and *n* values represent the longitudinal and circumferential modes respectively at which critical pressure appears. The calculated values for all models are presented in Table 4.

Here it can be seen that buckling modes for the specimens studied are $m = 1$ and $n = 3$ (one lobe in axial direction and three lobes around the circumference). A minimum buckling pressure is 6.3 MPa obtained by Flügge's model and a maximum buckling pressure of 8 MPa is obtained by Donnell's model.

Table 4

Buckling modes and pressures calculated by theoretical models

Model	*m*	*n*	*p* (MPa)
Modified Flügge model	1	3	6.9
Flügge model	1	3	6.3
Cheng et Ho model	1	3	6.3
Donnell model	1	3	8
Messager model	1	3	6.9

5. Experimental results

Fig. 11. Hyperbaric chamber (IFREMER Brest).

External pressure tests (13 tests in total) were carried out in a hyperbaric testing chamber (see Figure 11) at the IFREMER facilities in Brest. Four specimens (references 05VE5CNNI-22, 05VE1CNNI-25, 15VE1CNNI-29 and 15VE5CNNI-30) were instrumented with strain gages; four gages placed in the axial direction and four placed around the circumference, at mid-length on the inner wall. An angular separation of 45° was specified between consecutive gages, alternating axial and circumferential. Instrumented specimens were tested in axial compression under a small load (25 kN for thin walled cylinders and 100 kN for thick walled cylinders), on a 20 ton capacity test frame before pressure testing, in order to obtain axial mechanical material properties and to check that gages were functioning properly. The nomenclature chosen to describe specimens gives important information, and the meaning is as follows: The first two digits 05 or 15 (5mm or 15mm) indicate the nominal thickness of the specimen which actually is 4.4mm or 12.6mm. The third and fourth characters indicate the composite, in this case

VE means glass-epoxy composite. The fifth character (1 or 5) indicates the number of cells along the circumference. The sixth and seventh characters (CN) mean a normal curing cycle. The eighth and tenth characters indicate if specimens were instrumented with optical sensors or not (II or NI), in this cases all tested specimens were not instrumented (NI). The last two digits indicate a consecutive fabrication number.

For thin walled cylinders, it was assumed a uniform stress distribution along the thickness. Thick walled cylinders were exposed to same mechanical testing; gages were placed in the same positions as the thin walled ones, their experimental data was treated in the same way as the data for thin cylinders, and it was observed almost the same values for mechanical properties. So it was inferred that even if along the thickness of thick cylinders stress distribution is not uniform, for the dimensions of the thick cylinders used here, this stress variation along the thickness was not important, and could be neglected only to obtain mechanical properties in the elastic region, and assuming that the fiber fraction is almost the same in both cases (thin and thick cylinders).

5.1 Instrumented specimen results

Experimental mechanical properties from instrumented specimens are shown on Table 5. Axial properties (E_x, ν_{xy}) were obtained from axial compression tests, and circumferential properties (E_y and ν_{yx}) were deduced using pressure testing data combined with orthotropic laminate assumptions and axial mechanical properties. Experimental values were obtained using the mean response of gages.

Table 5
Experimental global mechanical properties

Thin walled specimens	E_x (MPa)	E_y (MPa)	ν_{xy}	ν_{yx}
05VE5CNNI-22	10711	18457	0.367	0.633
05VE1CNNI-25	10499	18449	0.373	0.656
Thin walled specimen mean values	10605	18453	0.370	0.645

Thick walled specimens	E_x (MPa)	E_y (MPa)	ν_{xy}	ν_{yx}
15VE1CNNI-29	9877	15955	0.370	0.598

15VE5CNNI-30	10711	16245	0.382	0.579
Thick walled specimen mean values	10294	16100	0.376	0.589

	E_x (MPa)	E_y (MPa)	ν_{xy}	ν_{yx}
Global mean values	10449	17277	0.373	0.617

With experimental mechanical properties (Table 5) *A* and *D* constants were calculated (experimental values), and results are shown in Table 3. The difference between experimental and calculated values is very small, in the range from 4 to 7 %.

Examples of pressure and strain response are presented in Figures 12 and 13 using data provided by instrumented specimens. It was noted that thin walled cylinders (05VE1CNNI-25 and 05VE5CNNI-22) show a buckling behavior starting at an external pressure between 5 and 6 MPa, for specimen 05VE1CNNI-25 the buckling pressure seems to be about 6 MPa, and for specimen 05VE5CNNI-22 buckling pressure is about 5.5 MPa. For the thick walled cylinders (15VE1CNNI-29, 15VE5CNNI-30) no buckling behavior is noted. In Figures 12 and 13 the average slope is almost the same between de gages placed in the same direction until shell instability begins when buckling modes are responsible for dramatic strain changes. During linear response the averaged pressure vs. strain diagram is still a straight line, small slope variations may be due to material variations, for example fluctuations in thickness.

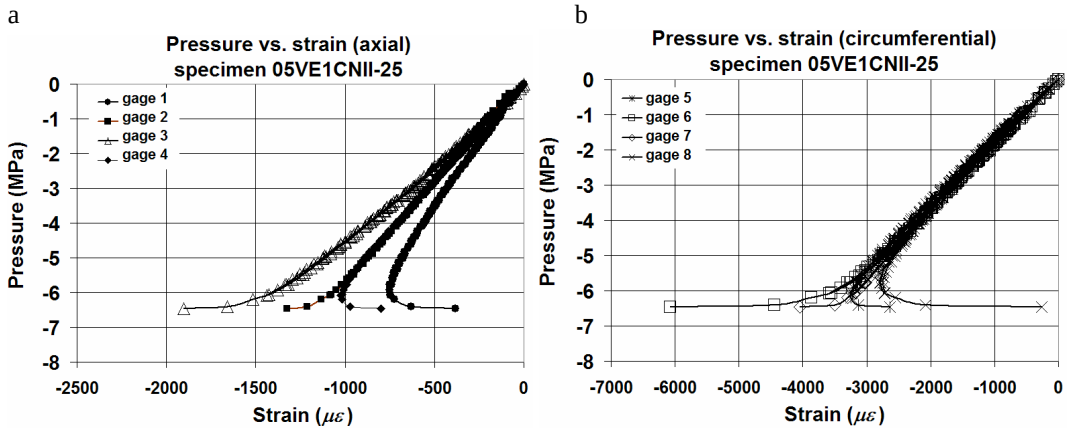

Fig. 12. Curves for thin specimen 05VE1CNII-25; (a) Pressure vs. axial strain, (b) Pressure vs. circumferential strain.

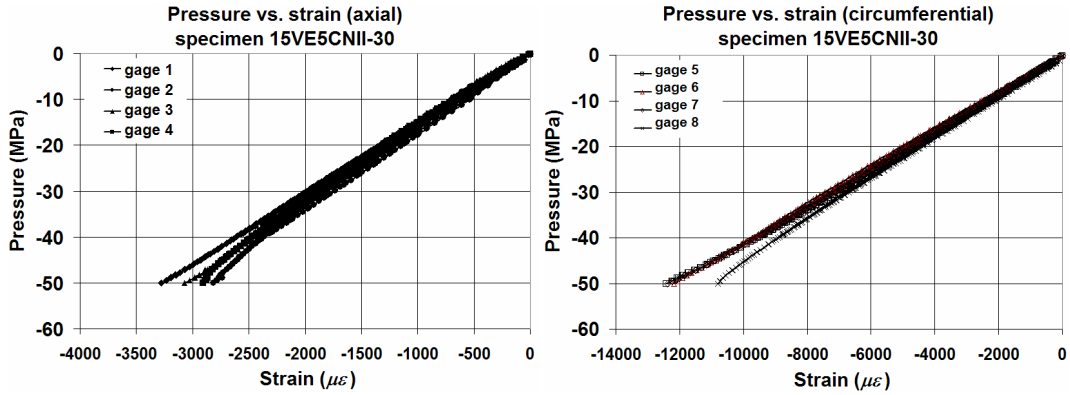

Fig. 13. Curves for thick specimen 15VE5CNII-30; (a) Pressure vs. axial strain, (b) Pressure vs. circumferential strain.

Comparing experimentally observed buckling pressures for thin walled cylinders with calculated pressures, it is seen that the models proposed by Cheng and Ho [6] and Flügge [5] provide predictions which are closest to experimental values.

5.2 Implosion results

In Table 6 the measured implosion pressure values are presented, as well as observed buckling modes. It may be noted that the mean implosion pressure for the 5 cell pattern specimens is 6.6 MPa, and for 1 cell pattern it is 6.5 MPa. The overall thin walled cylinder mean buckling pressure is 6.5 MPa, with a standard deviation of 0.4 MPa. It can therefore be stated that winding pattern has no influence on the implosion pressure of these thin walled cylinders.

Table 6
Implosion pressure for thin walled cylinders (mean thickness 4.4mm)

Specimen identification	Pattern (number of cells)	Implosion pressure (bar)	Mode
05VE5CNNI-10	5	60.0	2
05VE5CNNI-20	5	70.0	3
05VE5CNNI-21	5	65.0	3
05VE5CNNI-22	5	70.7	3
05VE5CNNI-23	5	64.0	3

4.4 mm mean thickness and 5 cell pattern specimens	Mean	65.9	
05VE1CNNI-15	1	60.0	2
05VE1CNNI-24	1	68.0	3
05VE1CNNI-25	1	64.7	3
05VE1CNNI-26	1	64.0	3
05VE1CNNI-27	1	67.0	3
4.4 mm mean thickness and 1 cell pattern specimens	Mean	64.7	
Thin walled specimens	Mean	65.3	
	Standard deviation	3.7	
	Coefficient of variation	0.1	
	Maximum	70.7	
	Minimum	60.0	
	Maximum - Minimum	10.7	
	Max - Min/Mean	0.2	

Results from thick walled cylinders (see Table 7) must be analyzed carefully, because of the small number of specimens. At first sight, the implosion value for the only 1 cell pattern specimen tested (52 MPa), appears to be higher by about 7 % than the mean value for the 5 cell pattern cylinders (48.4 MPa). One might expect the fibre undulations to reduce the compression strength [21] but further tests are needed to confirm this result.

After testing a post mortem analysis was made in order to observe morphological characteristics of damaged cylinders (buckling modes). Concerning buckling modes, it can be seen that for all thin walled cylinders a three circumferential lobe mode is present (see Figure 14). For thick walled specimens no

clear buckled shape is noted although the fracture pattern might suggest a mode 2 failure in the circumferential direction and mode 1 in the longitudinal direction (see Figure 15).

Table 7

Implosion pressure for thick walled cylinders (mean thickness 12.6 mm)

Specimen identification	Pattern (number of cells)	Implosion pressure (bar)	Mode
15VE1CNNI-29	1	520.6	2
15VE5CNNI-30	5	500.8	2
15VE5CNNI-31	5	467.0	2
12.6 mm mean thickness and 5 cell pattern specimens	Mean	483.9	
Thick walled specimens	Mean	496.1	
	Maximum	520.6	
	Minimum	467	

Fig. 14. Damaged thin walled specimen after implosion, showing buckling modes with mode one axial and mode 3 circumferential; (a) schematic view, (b) and (c) views of a buckled tube.

Calculated buckling modes from all models give the same result (see Table 4), $m = 1$ and $n = 3$, one lobe axial and three lobes in circumferential direction, this agrees with experimentally observed buckling modes (see Table 6, and Figure 14).

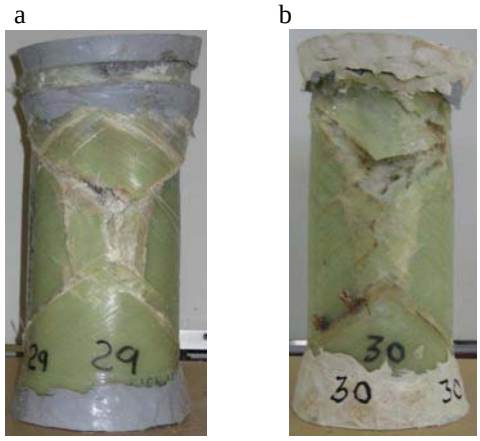

Fig. 15. Damaged thick walled specimens; (a) 1 unit cell pattern, (b) 5 unit cell pattern.

6. Conclusions

Results from this study show no strong influence of the two chosen winding patterns on the implosion pressure of filament wound composite cylinders. Buckling behavior does not seem to be sensitive to these two winding patterns. Buckling modes for specimen dimensions and characteristics used in this research are all of the $m = 1$ and $n = 3$ type, independent of winding pattern. Surface damage morphology of thick walled cylinders is not influenced by winding pattern. The choice of 1 and 5 unit cells along the circumference of cylindrical specimens is made, between several possibilities, for represent extreme cases (degree of undulation minimum or very high). Moreover, the coincidence of the unit cells through the thickness direction would have amplified the influence, if it had existed, of the unit cell size on mechanical behavior. For all that, if there is no clear influence of the winding pattern on implosion pressure and buckling behavior, we can think that this parameter don't have a major role in the resistance of filament wound cylinders under external pressure. All theoretical models predicted axial mode one ($m = 1$) and circumferential mode three ($n = 3$), which corresponds exactly to experimentally observed buckling modes. Buckling pressure evaluated using the Flügge [5] and Cheng and Ho models [6] provided the closest critical pressure predictions to the experimental buckling pressure. The different presented buckling behaviors of tubular structures depend on their thickness, but other geometrical parameters (different length-diameter ratios, etc) could have of course a direct influence on the buckling response too.

Acknowledgments

Hilario Hernández Moreno wishes to thank the National Council of Science and Technology of Mexico (CONACYT) and the National Polytechnic Institute of Mexico (IPN) for their scholarship sponsoring. The authors thank Mrs. Ivan Fernandez Hernandez, Jérémie Bauw, Felipe Afonso, and Erik Vargas Rojas for their collaboration during their internship at LGMT/PRO^{2}COM. Also many thanks to Mr. Matthieu Mulle, PhD at LGMT/PRO^{2}COM, for his collaboration during the instrumented implosion test, and IFREMER for its financial and technical support, with special thanks to Philippe Warnier and Albert Deuff.

References

1. Hoa SV. Analysis for design of fiber reinforced plastic vessels and piping. Technomic Publication: Lancaster, 1991.

2. Koussios S, Filament Winding: a Unified Approach, PhD Thesis, Delft University Press, Delft, 2004. p 1-300.

3. Zhao L,. Mantell SC, Cohen D, McPeak R, Finite element modeling of the filament winding process, Composite Structures, 2001, Vol. 52(3-4), p. 499-510.

4. Donnell LH. Stability of thin-walled tubes under torsion. NACA report No. 479, 1933. p. 95-116.

5. Flügge W. Stress in shells, 2nd edition. Springer-Verlag Berlin Heidelberg NewYork, 1973. p. 103-112, 204-217, 439-452.

6. Cheng S, Ho BPC. Stability of heterogeneous anisotropic cylindrical shells under combined loading. AIAA Journal, Vol. 1, 1963. p. 892-898.

7. Peterson JP, Seide P, Weingarten VI. Buckling of thin-walled circular cylinders. NASA SP 8007, 1968. p. 13-40.

8. Smitses G. Buckilng of moderately thick laminated cylindrical shells, a review. Composites: Part B, Vol. 27, 1996. p. 581-587.

9. Fuchs JP, Hyer MW, Starnes JH Jr. Numerical and experimental investigation of bending response of thin-walled composite cylinders. NASA CR 195730. Blacksburg, 1993.

10. Hahn HT, Jensen DW, Claus SJ, Pai SP, Hipp PA. Structural design criteria for filament-wound composite shells. NASA CR 195125, 1994.

11. Messager T. Buckling of imperfect laminated cylinders under hydrostatic pressure. Composite Structures, Vol. 53, 2001. p. 301-307.

12. Elghazouli AY, Chryssanthopoulos MK, Spagnoli A. Experimental response of glass-reinforced plastic cylinders under axial compression. Marine Structures, Vol. 11, 1998. p. 347–371.

13. Carvelli V, Panzeri N, Poggi C. Buckling strength of GFRP under-water vehicles. Composites: Part B, Vol. 32, 2001. p. 89-101.

14. Lowe A. Lecture notes for ENGN4511. Composite materials, Department of Engineering, Australian National University, Camberra, 2001. p. 52-53.

15. Lye SW, Boey FYC. Development of a low-cost prototype filament-winding system for composite components. Journal of Materials Processing Technology, Vol. 52, 1995. p. 570-584.

16. Berthelot JM. Matériaux composites. Tec & Doc, Paris, 1994. p. 63-67.

17. Shen FC. A filament-wound structure technology overview. Materials Chemistry and Physics, Vol. 42(2), 1995. p. 96-100.

18. International standard ISO 1268-5: 2001, Plastiques renforcés de fibre – Méthodes de fabrication de plaques d'essai - Partie 5: Moulage par enroulement filamentaire, première édition. Organisation Internationale de Normalisation. Genève, 2001.

19. Daniel IM, Ishai O. Engineering mechanics of composite materials. Oxford University Press, 1994.

20. Hernandez-Moreno H. Monitoring de la fabrication de tubes composites réalisés par enroulement filamentaire et comportement mécanique sous pression externe. PhD Thesis, Université Paul Sabatier (in French), 2006, p. 1-238.

21. Hsiao HM, Daniel IM. Effect of fiber waviness on stiffness and strength reduction of unidirectional composites under compressive loading. Composites Science and Technology, 1996, Vol. 56(5), p 581-593.